

Pharmacokinetic assessment of ^{18}F -(2S,4R)-4-fluoroglutamine in patients with cancer

Milan Grkovski¹, Reema Goel², Simone Krebs², Kevin D. Staton³, James J. Harding⁴, Ingo K. Mellinghoff⁵, John L. Humm¹, Mark P.S. Dunphy²

¹Department of Medical Physics, Memorial Sloan Kettering Cancer Center, New York, NY

²Department of Radiology, Memorial Sloan Kettering Cancer Center, New York, NY

³Radiochemistry & Molecular Imaging Probe Core Facility, Memorial Sloan Kettering Cancer Center, New York, NY

⁴Department of Medicine, Memorial Sloan Kettering Cancer Center, New York, NY

⁵Department of Neurology, Memorial Sloan Kettering Cancer Center, New York, NY

Running title: ^{18}F -fluoroglutamine dynamic PET

Financial support: This research was funded in part by the David Mahoney Neuroimaging Program of the Dana Foundation, the Paul Calabresi Career Development Award for Clinical Oncology (K12 CA184746), the National Cancer Institute (P50 CA086438, R01 CA164490, R01 CA172546, R21 CA167803, and R01 CA204093), and Stand Up To Cancer (grant SU2C-AACRDT0509). MSKCC's core facilities are supported by the NIH/NCI Cancer Center Support Grant (P30 CA008748).

Corresponding Author:

Mark P.S. Dunphy, DO
Molecular Imaging and Therapy Service
Department of Radiology
Memorial Sloan Kettering Cancer Center
1275 York Avenue
New York, NY 10065
Phone: 212-639-8131
Email: dunphym@mskcc.org

Conflicts of Interest: J.J.H. has received consulting fees unrelated to the current work from Bristol-Myers Squibb, Eisai, Eli Lilly, and CytomX and research support from Bristol-Myers Squibb. No other potential conflicts of interest relevant to this article exist.

Word count: 4995

ABSTRACT

^{18}F -(2S,4R)-4-fluoroglutamine (^{18}F -FGln) is an investigational positron emission tomography (PET) radiotracer for imaging tumor glutamine flux and metabolism. The aim of this study was to investigate its pharmacokinetic properties in patients with cancer.

Methods: Fifty lesions from 41 patients (21M/20F, aged 54 ± 14 years) were analyzed. 30-min dynamic PET scans were performed concurrent with a rapid intravenous bolus injection of 232 ± 82 MBq of ^{18}F -FGln, followed by two static PET scans at 97 ± 14 min and 190 ± 12 min post-injection. Five patients also underwent a second ^{18}F -FGln study 4-13 weeks after initiation of therapy with either glutaminase, dual TORC1/2, or PD-1 inhibitors. Blood samples were collected to determine plasma and metabolite fractions and to scale the image-derived input function. Regions of interest were manually drawn to calculate standardized uptake values (SUVs). Pharmacokinetic modeling with both reversible and irreversible one- and two-tissue compartment models was performed to calculate kinetic rate constants K_1 , k_2 , k_3 , and k_4 . The analysis was repeated with truncated 30-min dynamic datasets.

Results: Intratumor ^{18}F -FGln uptake patterns demonstrated substantial heterogeneity in different lesion types. In majority of lesions, reversible two-tissue compartment model was chosen as the most appropriate according to the Akaike Information Criterion. K_1 , a surrogate biomarker for ^{18}F -FGln intracellular transport, was the kinetic rate constant that was most correlated with both SUV at 30-min (Spearman's $\rho=0.71$) and with SUV at 190-min ($\rho=0.51$). Only K_1 was reproducible from truncated 30-min datasets (ICC=0.96). k_3 , a surrogate biomarker for glutaminolysis rate, was relatively low in ~50% of lesions. Treatment with glutaminase inhibitor CB-839 substantially reduced the glutaminolysis rates as measured by k_3 .

Conclusion: ^{18}F -FGln dynamic PET is a sensitive tool for studying glutamine transport and metabolism in human malignancies. Analysis of dynamic data facilitates better understanding of ^{18}F -FGln pharmacokinetics and may be necessary for response assessment to targeted therapies that impact intracellular glutamine pool size and tumor glutaminolysis rates.

Keywords: Glutamine, metabolism, glutaminolysis, dynamic PET, kinetic modeling

INTRODUCTION

Glutamine, alongside glucose, is one of two principal nutrients that support survival, biosynthesis, and cellular homeostasis in mammalian cells, thus playing an essential role in cancer cell metabolism (1-5). The glutaminolytic pathway is highly active in many aggressive cancers (6). ^{18}F -(2S,4R)-4-fluoroglutamine (^{18}F -FGln) is an L-glutamine analog that was developed as an investigational positron emission tomography (PET) radiopharmaceutical for imaging tumor glutamine flux and metabolism (7,8). Non-invasive clinical assays for imaging tumor glutamine metabolic pathways can provide complementary value to ^{18}F -fluorodeoxyglucose (^{18}F -FDG) PET in several scenarios (9): (i) The ability of tumors to preferentially utilize glutamine suggests that glutaminolysis may be the metabolic pathway present in ^{18}F -FDG-negative tumors (2,8,10); (ii) ^{18}F -FGln may be useful for identifying residual viable tumor in patients on drug regimens that suppress glucose uptake such as inhibitors of PI3K/AKT/mTOR pathway (11,12); (iii) Visualization of ^{18}F -FDG-avid tumors is difficult if the physiological ^{18}F -FDG uptake in normal surrounding tissue is comparable to that of the tumor, as is the case in the cerebral cortex (13). Due to low glutamine consumption in normal brain tissue, ^{18}F -FGln provides higher tumor-to-background ratios than ^{18}F -FDG (14); (iv) Imaging of glutamine metabolism might carry prognostic value as a metabolic marker of tumor aggressiveness (15); and (v) Many different mutations can lead to enhanced glucose uptake. Identifying a subset of tumors with enhanced glutamine metabolism such as those with c-Myc amplification (4,5,16) could allow for the prediction of specific genetic alterations, facilitating patient stratification for targeted therapy trials and personalized treatment monitoring. For example, glutaminase, an amidohydrolase enzyme that generates glutamate from glutamine, is the rate-limiting enzyme in glutaminolysis. It is upregulated by the oncogene c-Myc (9), which can lead to glutamine addiction (2). The exploitation of the glutaminolysis pathway for therapeutic purposes is spurring research into glutaminase inhibitors as potential cancer therapeutic targets (17); (vi) Furthermore, cancer cells may use both PI3K/Akt/mTOR and c-Myc pathways to generate energy for growth and survival (8). Adding ^{18}F -FGln PET would provide a more complete picture of tumor metabolism than imaging with ^{18}F -FDG alone (6).

^{18}F -FGln has recently been clinically validated as a promising tumor biomarker in several different cancer types (14,15). The objectives of this study were to investigate the pharmacokinetic properties of ^{18}F -FGln and to evaluate the added benefit of dynamic over simpler static ^{18}F -FGln PET.

MATERIALS AND METHODS

Patient Selection

The data presented in this study was acquired as a part of an open-label, nonrandomized, microdose phase I trial of ^{18}F -FGln. The trial was approved by Memorial Sloan Kettering Cancer Center's Institutional Review Board and conducted under a Food and Drug Administration-approved Investigational New Drug application (ClinicalTrials.gov Identifier: NCT01697930). The study was conducted in accordance with the Helsinki Declaration and the Health Insurance Portability and Accountability Act. Patients provided written informed consent before participating in the study. Subject inclusion criteria included: (i) age of 21–90 years; (ii) serum renal and hepatic function test values less than 1.5–2.5-fold greater than the laboratory-specific upper limit of normal, histologically confirmed cancer; and (iii) tumors visualized with standard imaging (computed tomography [CT], magnetic resonance [MR], and/or ^{18}F -FDG PET/CT) performed less than four weeks before consent. Serum complete blood count and hepatorenal function tests were performed less than two weeks before study participation. Patients were excluded if they were pregnant, breastfeeding, or had an acute major illness.

PET/CT Imaging

^{18}F -FGln was synthesized by Memorial Sloan Kettering Cancer Center's Radiochemistry and Molecular Imaging Probe Core Facility as described previously (15). Each ^{18}F -FGln dose met drug product acceptance specifications, including radiochemical purity and identity, residual solvent content, endotoxin content, radionuclidic identity, pH, and appearance.

Dynamic PET scans were performed over a single field of view (FOV; 15.7 cm axially) on the Discovery STE, 690 or 710 cameras (GE Health Care, Inc.), concurrent with a rapid intravenous bolus injection of 232 ± 82 MBq of ^{18}F -FGln (range, 29–469 MBq). Images were acquired in list mode and binned into 12×10 -

sec, 3×60-sec and 5×300-sec, for a total of 30-min. A CT scan (120 kVp, 70 mA, and 3.8-mm slice thickness) was obtained for attenuation correction, anatomical localization and co-registration purposes. Dynamic acquisition was followed by two static PET scans starting at 97±14 min and 190±12 min post-injection (15-30 min acquisition time). PET emission data were acquired in three-dimensional mode; corrected for attenuation, scatter, and random events; and iteratively reconstructed into either a 256×256×47 matrix (voxel dimensions: 1.95×1.95×3.27 mm³, for brain lesions) or 128×128×47 matrix (voxel dimensions: 2.34×2.34×3.27 mm³, for lesions in thoracic and abdominal area) using the ordered subset expectation maximization algorithm provided by the manufacturer. For 5 patients, second dynamic ¹⁸F-FGln PET scans were also performed on the same scanner, 4-13 weeks after starting a new anti-cancer treatment with either glutaminase, dual TORC1/2, or PD-1 inhibitors.

Blood Sample Analysis

Activity in whole blood and plasma specimens was radioassayed with a calibrated well counter (1480 Wallac Wizard 3 Automatic Gamma Counter (Perkin Elmer, Inc.)) after separating blood and plasma by centrifuge (4000 rpm for 10 minutes at 4°C), as described previously (15). Multiple venous blood samples were obtained between 5 and 180 min post-injection. The measured activity concentrations were converted to kBq/cc. Metabolite analysis of activity in plasma was performed by reversed phase high-performance liquid chromatography with in-line radiation detection on samples obtained up to 65 min after injection.

Image Analysis

All three PET segments were spatially co-registered using the rigid-body transformation calculated with General Co-Registration™ tool (General Electric Advantage Workstation v4.7) applied to their corresponding CT scans to form a concatenated ¹⁸F-FGln dynamic PET. Subsequent processing was performed in PMOD v3.604 (PMOD Software, RRID:SCR_016547). Regions of interest (ROIs) were drawn over sites of disease identified by a radiologist with experience in nuclear medicine. Time-activity curves (TAC) and standardized uptake values corrected by body weight (SUV_{bw}) were derived from lesions. For each patient with a brain lesion, analysis was also performed for normal brain tissue by averaging the results from 10 spherical ROIs each with a 10-mm radius.

Input function was image-derived by manually defining an ROI over the internal carotid artery or descending aorta on the early frame with the highest image intensity. For each patient, whole-blood input function TACs were scaled by the whole-blood activity concentration as measured from blood samples and corrected for plasma fraction. Metabolite counts were analyzed in only a subset of patients; therefore, an averaged population-based metabolite correction was applied for all patients.

Pharmacokinetic Modeling

Irreversible and reversible one-compartment (1C1K and 1C2K, respectively) and two-tissue compartment (2C3K and 2C4K, respectively) pharmacokinetic models with a blood fraction component (v_B) were investigated to calculate kinetic rate constants K_1 , k_2 , k_3 and k_4 . In the 2C4K model (Figure 1), K_1 is assumed to be a surrogate biomarker for perfusion, tumor vascular permeability and intracellular transport rate mediated by ASCT2. k_3 , on the other hand, may be a surrogate biomarker for the first and rate-limiting step of glutaminolysis that is catalyzed by glutaminase and yields ^{18}F -fluoroglutamate. Further downstream processes in the glutaminolytic pathway (e.g., metabolization of ^{18}F -fluoroglutamate to ^{18}F -fluoro- α -ketoglutarate) are likely also incorporated into k_3 . In this framework, k_2 represents the efflux back into vasculature, whereas k_4 represents either the excretion of ^{18}F -Fluoroglutamate, efflux of free ^{18}F (a by-product of the metabolization of ^{18}F -fluoroglutamate to α -ketoglutarate by alanine aminotransferase (18)) or conversion of ^{18}F -Fluoroglutamate back into ^{18}F -Fluoroglutamine by glutamine synthetase (19).

The total concentration of activity measured by the PET scanner as a function of time t post-injection, $C(t)$, is given by

$$C(t) = v_B C_p(t) + (1 - v_B)(C_1(t) + C_2(t)), \quad (1)$$

where $C_p(t)$ is the activity concentration of the unmetabolized radiotracer in the plasma, whereas $C_1(t)$ and $C_2(t)$ are the activity concentrations associated with the first and second compartment, corresponding to non-specifically and specifically bound radiotracer in tissue. The rate of change for $C_1(t)$ and $C_2(t)$ is described by the system of differential equations:

$$\frac{dC_1(t)}{dt} = K_1 C_p(t) - (k_2 + k_3)C_1 + k_4 C_2(t), \quad (2)$$

$$\frac{dC_2(t)}{dt} = k_3 C_1(t) - k_4 C_2(t). \quad (3)$$

Default starting parameter values for K_1 , k_2 , k_3 and k_4 were 0.1 mL/min/g, 0.1 min⁻¹, 0.1 min⁻¹ and 0.1 min⁻¹, respectively (in all cases, lower and upper bounds were 0 and 8, respectively). Goodness of fit was evaluated with Akaike Information Criterion to determine the most appropriate compartmental model. Volume of distribution, V_T , was calculated as

$$V_T = \frac{K_1}{k_2} \left(1 + \frac{k_3}{k_4} \right). \quad (4)$$

Logan graphical analysis (20), a technique originally developed for calculating the volume of distribution of reversible receptor systems, was also performed.

To evaluate the utility of truncated ¹⁸F-Gln datasets, tumor TACs derived from the first 30-min of data were refitted with the 2C4K model. All metrics as calculated with truncated datasets were compared to those derived from full datasets.

Statistical Analysis

The correlation strength between different indices was analyzed using Spearman's rank correlation coefficient ρ . Comparisons of metrics as calculated from different patient sub-groups were performed with unpaired two-tailed *t*-test. Bland-Altman analysis was performed to estimate the mean difference between parameters as calculated with full and truncated datasets and 95% limits of agreement. Reproducibility of metrics calculated from different methods was evaluated using two-way random single score Intraclass Correlation Coefficient (ICC). $p < 0.05$ was assumed to represent statistical significance.

RESULTS

Sixty-five patients were enrolled in the study between January 2013 and October 2018. Of these, 11 patients subsequently withdrew consent and for 13 patients, dynamic ¹⁸F-FGln PET images were not analyzed due to the absence of lesions within the field of view of the dynamic scan ($n=7$) or corrupt or lost dynamic PET data ($n=6$). Forty-one patients (21M/20F; aged 54 ± 14 years, range: 24-80 years) and 50 lesions in total were included in the analysis (Table 1). For 28 of the 41 patients, FOV was focused over

the brain (Subgroup 1; n=35 lesions), whereas for the remaining 13 patients, FOV was focused over the thoracic or abdominal region (Subgroup 2; n=15 lesions). Lesions measured $4.2 \pm 7.5 \text{ cm}^3$ (range, 0.2-36.9 cm^3). The percentage of activity due to ^{18}F -FGln in plasma was $78 \pm 12\%$, $80 \pm 13\%$, $78 \pm 11\%$, $76 \pm 9\%$, $73 \pm 8\%$, and $69 \pm 9\%$ at 2, 6, 16, 30, 65, and 158 min after injection, respectively (n=44 patients with available blood data). Metabolite analysis at multiple time-points was performed for a subset of patients, from which a population-based metabolite correction function was derived. Unmetabolized ^{18}F -FGln fraction was $78 \pm 10\%$ (n=9 data points), $75 \pm 12\%$ (n=4), $73 \pm 11\%$ (n=28), and $59 \pm 7\%$ (n=5) at 2, 6, 30, and 65 min after injection.

According to the Akaike Information Criterion, the 1C2K, 2C3K, and 2C4K models were most appropriate in 9, 15, and 26 lesions, respectively. Across 50 lesions, AIC values were 160 ± 30 , 146 ± 29 and 141 ± 28 , respectively. Lesions for which 1C2K or 2C3K were deemed better than 2C4K model exhibited k_3 and/or k_4 values close to zero, therefore adding these fitting parameters did not improve the fit. In the majority of lesions, goodness of fit was perceptibly poorer when 1C2K or 2C3K models were used. Therefore, only results obtained with a 2C4K model are presented.

Pharmacokinetic modeling of ^{18}F -FGln dynamic PET with a 2C4K model are summarized in Table 2. Also included are the results for all brain lesions (subgroup 1), primary brain lesions (subgroup 1A), brain metastases (subgroup 1B) and all thoracic/abdominal lesions (subgroup 2), as well as for normal brain tissue. ^{18}F -FGln uptake in tumors was rapid and subsequently decreased. Compared to ^{18}F -FGln tumor uptake, ^{18}F -FGln uptake in normal brain tissue was significantly lower at all imaging time-points. Analysis was also repeated for ROIs encompassing the small area (5 voxels) with the highest ^{18}F -FGln uptake (Supplementary Table S1). V_T as calculated from Logan graphical analysis and 1C2K model were strongly correlated (ICC=0.95; $V_T=3.7 \pm 1.7 \text{ mL/cm}^3$ and $V_T=4.0 \pm 2.0 \text{ mL/cm}^3$ respectively). Correlation was lower for V_T calculated from 2C4K model, ICC=0.80 ($V_T=4.5 \pm 2.4 \text{ mL/cm}^3$). Among kinetic rate constants, K_1 was most closely correlated with SUV (Table 3).

K_1 -SUV1 and k_3 -SUV3 scatterplots are presented in Figs. 2A and 2B. Waterfall charts for these four metrics (Figs. 2C and 2D) revealed a wide range of observed values. k_3 was relatively low in ~50% of cases, indicating that glutaminolysis rates are not elevated in all lesions. Two ^{18}F -FGln uptake patterns were

observed (Fig. 3 and Supplementary Fig. S1A). In 29 out of 42 evaluable lesions (69%; in some patients, ^{18}F -FGln scans were not performed at all imaging time-points), ^{18}F -FGln SUV was highest around 30-min post-injection and decreased afterwards (Pattern 1). The remaining 13 lesions (31%; all in brain) exhibited a peak around 100-min imaging time-point with a subsequent decrease (Pattern 2). K_1 was significantly different between lesions exhibiting the two patterns ($K_1=0.19\pm0.13$ mL/min/g and $K_1=0.08\pm0.05$ mL/min/g, respectively; 2-tailed t-test, $p=0.01$). All $n=9$ lesions in five patients with brain metastases exhibited Pattern 2 (Supplementary Figure S1B).

The first compartment (assumed to represent ^{18}F -fluoroglutamine that has been transported from the vasculature and into the cell by ASCT2 but has not been converted to ^{18}F -Fluoroglutamate) contributed $76\pm14\%$, $65\pm25\%$, $52\pm24\%$, and $46\pm23\%$ of PET signal at 5, 30, ~ 100 and ~ 190 -min post-injection, respectively, whereas the contribution from the second compartment (representing ^{18}F -fluoroglutamate but also the incorporation of ^{18}F -fluoroglutamine into proteins) was $10\pm13\%$, $29\pm26\%$, $44\pm24\%$, and $50\pm23\%$, respectively (Supplementary Fig. S2).

Reproducibility analysis is summarized in Table 4. The intraclass correlation coefficient was highest for K_1 , which can be estimated from the initial 30-min segment of time-activity curves; however, none of the other kinetic rate constants were reproducible.

A total of five patients also underwent a second ^{18}F -FGln dynamic PET scan after therapy either with CB-839, a glutaminase inhibitor; TAK-228, a dual TORC1/2 inhibitor; or PD-1 inhibitors nivolumab or pembrolizumab (Table 5). Eight lesions were analyzed in these 5 patients, with the results summarized in Table 6. The effect of these treatments on glutaminolysis rate as measured by k_3 is illustrated in Figure 4A. Therapy with CB-839 resulted in a markedly decreased rate of glutaminolysis (i.e., k_3 fell to almost zero). A gradual decrease was also observed for a patient who received therapy with dual TORC1/2 inhibitor TAK-228. On the other hand, therapy with PD-1 inhibitors nivolumab and pembrolizumab seem to have increased the rate of glutaminolysis. Corresponding scatter-plot for SUV1 (Figure 4B) indicates greater ambiguity in interpreting the effects of therapies on ^{18}F -FGln uptake. An example of a glioblastoma multiforme patient imaged 13 weeks after initiation of treatment with nivolumab and radiotherapy is included in Figure 5. For this patient, elevated ^{18}F -FGln uptake and retention was hypothesized to be due to the

increased rate of glutaminolysis (an increased contribution to the signal from the second compartment), as the activity concentration associated with the first compartment remained similar. On the other hand, treatment with CB-839 in a patient with metastatic renal cell carcinoma appears to have reduced the rate of glutaminolysis as assessed by marked decrease in k_3 and decreased signal from the second compartment (Figure 6).

DISCUSSION

We investigated the pharmacokinetic properties of ^{18}F -FGln across lesions of different etiologies and demonstrate the added benefit of incorporating dynamic ^{18}F -FGln PET acquisitions into analysis. ^{18}F -FGln is readily imported into glutaminolytic tumor cells at rates comparable to ^{18}F -FDG (7). It is mainly transported across the cell membrane by the amino acid transporter ASCT2 (8,21,22). While ^{18}F -FGln uptake in normal brain was low due to minimal expression of ASCT2 (14), high variability was observed in surrogate metrics of glutamine transport (K_1 and SUV1) and retention (k_3 and SUV3) in lesions. Additionally, relevant tumor genetic alterations in genes that are key regulators of tumor glutamine flux and metabolism were found in several patients with ^{18}F -FGln-avid tumors (15).

Two ^{18}F -FGln tumor uptake patterns were noted: (i) initial rapid accumulation with a plateau around 30 min post-injection and a subsequent steep decrease; and (ii) slower accumulation with a plateau around 100 min post-injection and more gradual decrease. All brain metastases exhibited the second pattern, in agreement with a recent report (23). Despite similar K_1 between primary brain lesions and brain metastases (increased blood-brain barrier permeability does not significantly contribute to ^{18}F -FGln uptake; (14)), the latter exhibited fourfold higher k_3 , resulting in more sustained retention. Metabolic reprogramming of glutaminolysis was reported to mediate metastatic phenotype in lung cancer (24) and melanoma (25).

^{18}F -FGln uptake patterns might be important in understanding responses to targeted therapies with inhibitors of glutaminase (17) or ASCT2 (26), and cannot be readily elucidated using only static PET. The contributions from different processes to the total PET signal may, however, be uncoupled through analysis of dynamic PET data. A drawback of this approach is a clinically challenging acquisition protocol. Several

factors contribute to the intratumor uptake of ^{18}F -FGln, including upregulation of ASCT2 (resulting in higher K_1 and SUV1) and increased protein synthesis and glutaminolysis (resulting in higher k_3). However, increased glutaminase activity has also been associated with a smaller cellular glutamine pool size, which resulted in low tracer retention as ^{18}F -FGln competed with a small pool of native glutamine for efflux (6). Consequently, only weak correlation was observed between k_3 and SUV3. The typical time-course of ^{18}F -FGln accumulation in lesions precludes the use of truncated 30-min dynamic acquisitions, as the rate of glutaminolysis cannot be readily estimated from the available temporal information. Of note, k_3 was also not found to be correlated with the change in SUV (Table 3).

Reversibility of ^{18}F -FGln uptake has been suggested previously (6) and has also been observed in our study. However, a fraction of the radiotracer might be at least temporarily trapped within cells. Lieberman et al. demonstrated that ^{18}F -FGln showed significant in vivo incorporation to a trichloroacetic acid precipitated fraction, likely associated with intracellular protein or macromolecule synthesis, suggesting that this might be an important mechanism for radiotracer entrapment in tumors (8).

Targeted therapy with CB-839, a glutaminase inhibitor, resulted in a marked decrease in k_3 , consistent with the hypothesis that k_3 is a surrogate biomarker of glutaminolysis. Of note, ~50% of all lesions did not demonstrate elevated glutaminolysis levels according to k_3 , implicating that in these cases, targeted therapy with glutaminase inhibitors may not be effective. The patient highlighted in Figure 5 did however exhibit high levels of glutaminolysis at baseline (preclinical evidence of addiction of renal cell carcinoma cells to glutamine and glutaminase activity has been recently reviewed; (27)). All four lesions from the two patients that received CB-839 also exhibited marked decrease in k_2 (from $0.19 \pm 0.10 \text{ min}^{-1}$ on baseline to $0.08 \pm 0.04 \text{ min}^{-1}$ on follow-up) despite no substantial changes in K_1 (from $0.29 \pm 0.10 \text{ mL/min/g}$ to $0.26 \pm 0.20 \text{ mL/min/g}$) or SUV at 30-min (from 3.1 ± 0.5 to 3.2 ± 0.5), likely as ^{18}F -FGln competed with a larger pool of native glutamine molecules for efflux after glutaminase inhibition (6). Decrease in k_3 was also observed after therapy with a dual TORC1/2 inhibitor TAK-228, as the inhibition of mTORC1 activity suppresses the conversion of glutamine to α -ketoglutarate (28). On the other hand, treatment with nivolumab and pembrolizumab, human IgG4 anti-PD-1 monoclonal antibodies that work as checkpoint inhibitors and are believed to often provoke tumor inflammation when effective (29), led to an elevated glutaminolysis rate as

reflected in higher k_3 . Albina et al. reported that the intracellular free glutamine concentration is decreased in inflammation and the cellular components of the inflammatory infiltrate might be capable of active glutaminolysis (30).

Our study has several limitations: (i) Multiple patients received systemic anticancer treatments during or recently before ^{18}F -FGln PET, potentially reducing tumor ^{18}F -FGln avidity (14); (ii) The number of patients undergoing two ^{18}F -FGln studies was small, lowering the confidence in interpreting the effects of therapies on glutamine flux and metabolism. (iii) Radiochemical testing before ^{18}F -FGln injection confirmed the presence of <20% of stereoisomer, (2*R*,4*R*)-4- ^{18}F -fluoroglutamine, which, as an analogue of D-glutamine, is not avidly accumulated by tumor cells (7); (iv) Since fractions of unmetabolized radiotracer were not determined for all patients, population-derived metabolite correction was implemented instead; (v) The 2C4K model assumes that free ^{18}F is not significantly accumulated in tumors. While metabolite analyses confirmed in vivo production of free ^{18}F metabolite, hindering the analysis of tumors that are close to bone (15), Zhou and colleagues reported that the contribution of labeled metabolites to the tumor PET signal in mice is small ($\leq 10\%$) and unlikely to have a significant influence on image-derived metrics (6). We repeated the analysis utilizing a 3-compartment pharmacokinetic model with two input functions that accounts for non-specific uptake of radiometabolites, the contribution to the total signal from the 3rd compartment was $\sim 10\%$ (range, 0-20%), similar to the results reported by Zhou and colleagues (6). On the other hand, the percentage signal from the 3rd compartment was $>85\%$ in bone tissue, which is expected due to accumulation of free ^{18}F ; (vi) The accuracy and precision of kinetic rate constant prediction is susceptible to experimental levels of noise. Exploratory Monte Carlo simulations (Supplementary Methods) indicate that the calculation of K_1 and k_2 is relatively robust, whereas k_3 and k_4 exhibit higher variance in cases where their true values are very low; (vii) Moderate correlation between K_1 and k_3 (Supplementary Table S2) suggests that ASCT2 and glutaminase activity may both be upregulated in tumors. An alternative interpretation, however, is that the 2C4K model cannot reliably uncouple contributions from different compartments to the total PET signal, *i.e.*, the kinetic rate constants are not identifiable.

CONCLUSION

^{18}F -FGln dynamic PET is a sensitive tool for studying glutamine transport and metabolism in human malignancies. Analysis of dynamic data facilitates better understanding of ^{18}F -FGln pharmacokinetics and may be necessary for response assessment to targeted therapies that impact intracellular glutamine pool size and tumor glutaminolysis rates.

Acknowledgements: The authors thank Leah R. Bassity for editorial comments on this manuscript.

Disclosure: This research was funded in part by the David Mahoney Neuroimaging Program of the Dana Foundation, the Paul Calabresi Career Development Award for Clinical Oncology (K12 CA184746), the National Cancer Institute (P50 CA086438, R01 CA164490, R01 CA172546, R21 CA167803, and R01 CA204093), and Stand Up To Cancer (grant SU2C-AACRDT0509). MSKCC's core facilities are supported by the NIH/NCI Cancer Center Support Grant (P30 CA008748). J.J.H. has received consulting fees unrelated to the current work from Bristol-Myers Squibb, Eisai, Eli Lilly, and CytomX and research support from Bristol-Myers Squibb. No other potential conflicts of interest relevant to this article exist.

KEY POINTS

Question: To assess the suitability of ^{18}F -(2S,4R)-4-fluoroglutamine as a PET radiotracer for imaging tumor glutamine flux and metabolism.

Pertinent findings: Analysis of dynamic ^{18}F -(2S,4R)-4-fluoroglutamine PET data facilitates better understanding of the heterogeneous uptake patterns of ^{18}F -(2S,4R)-4-fluoroglutamine, due to uncoupling of the total PET signal into contributions from: (i) perfusion, vascular permeability and ASCT2-mediated intracellular transport; and (ii) rate-limiting step of glutaminolysis that is catalyzed by glutaminase.

Implications for patient care: Incorporation of pharmacokinetic modeling of dynamic ^{18}F -(2S,4R)-4-fluoroglutamine PET may be necessary for response assessment to targeted therapies that impact intracellular glutamine pool size and tumor glutaminolysis rates.

REFERENCES

1. Vander Heiden MG, Cantley LC, Thompson CB. Understanding the Warburg effect: the metabolic requirements of cell proliferation. *Science*. 2009;324:1029-1033.
2. Wise DR, DeBerardinis RJ, Mancuso A, et al. Myc regulates a transcriptional program that stimulates mitochondrial glutaminolysis and leads to glutamine addiction. *Proc Natl Acad Sci U S A*. 2008;105:18782-18787.
3. Altman BJ, Stine ZE, Dang CV. From Krebs to clinic: glutamine metabolism to cancer therapy. *Nat Rev Cancer*. 2016;16:619-634.
4. Zhang J, Pavlova NN, Thompson CB. Cancer cell metabolism: the essential role of the nonessential amino acid, glutamine. *EMBO J*. 2017;36:1302-1315.
5. Yang L, Venneti S and Negrath D. Glutaminolysis: A Hallmark of Cancer Metabolism. *Annu Rev Biomed Eng*. 2017;19:163-194.
6. Zhou R, Pantel AR, Li S, et al. [^{18}F](2S,4R)4-Fluoroglutamine PET Detects Glutamine Pool Size Changes in Triple-Negative Breast Cancer in Response to Glutaminase Inhibition. *Cancer Res*. 2017;77:1476-1484.
7. Qu W, Zha Z, Ploessl K, et al. Synthesis of optically pure 4-fluoro-glutamines as potential metabolic imaging agents for tumors. *J Am Chem Soc*. 2011;133:1122-1133.
8. Lieberman BP, Ploessl K, Wang L, et al. PET imaging of glutaminolysis in tumors by 18F-(2S,4R)4-fluoroglutamine. *J Nucl Med*. 2011;52:1947-1955.
9. Rajagopalan KN and DeBerardinis RJ. Role of glutamine in cancer: therapeutic and imaging implications. *J Nucl Med*. 2011;52:1005-1008.
10. Gao P, Tchernyshyov I, Chang TC, et al. c-Myc suppression of miR-23a/b enhances mitochondrial glutaminase expression and glutamine metabolism. *Nature*. 2009;458:762-765
11. LoPiccolo J, Blumenthal GM, Bernstein WB and Dennis PA. Targeting the PI3K/Akt/mTOR pathway: effective combinations and clinical considerations. *Drug Resist Updat*. 2008;11:32-50.
12. Yang C, Sudderth J, Dang T, Bachoo RM, McDonald JG and DeBerardinis RJ. Glioblastoma cells require glutamate dehydrogenase to survive impairments of glucose metabolism or Akt signaling. *Cancer Res*. 2009;69:7986-7993.
13. Fink JR, Muzi M, Peck M and Krohn KA. Multimodality Brain Tumor Imaging: MR Imaging, PET, and PET/MR Imaging. *J Nucl Med*. 2015;56:1554-1561.
14. Venneti S, Dunphy MP, Zhang H, et al. Glutamine-based PET imaging facilitates enhanced metabolic evaluation of gliomas in vivo. *Sci Transl Med*. 2015;7:274ra17.
15. Dunphy MPS, Harding JJ, Venneti S, et al. In Vivo PET Assay of Tumor Glutamine Flux and Metabolism: In-Human Trial of 18F-(2S,4R)-4-Fluoroglutamine. *Radiology*. 2018;287:667-675.
16. Wise DR, Thompson CB. Glutamine addiction: a new therapeutic target in cancer. *Trends Biochem Sci*. 2010;35:427-433.
17. Gross MI, Demo SD, Dennison JB, et al. Antitumor activity of the glutaminase inhibitor CB-839 in triple-negative breast cancer. *Mol Cancer Ther*. 2014;13:890-901.
18. Cooper AJ, Krasnikov BF, Pinto JT, Kung HF and Ploessl K. Comparative enzymology of (2S,4R)4-fluoroglutamine and (2S,4R)4-fluoroglutamate. *Comp Biochem Physiol B Biochem Mol Biol*. 2012;163:108-120.

19. Tardito S, Oudin A, Ahmed SU, et al. Glutamine synthetase activity fuels nucleotide biosynthesis and supports growth of glutamine-restricted glioblastoma. *Nat Cell Biol.* 2015 ;17:1556-1568
20. Logan J, Fowler JS, Ding YS, et al. Strategy for the formation of parametric images under conditions of low injected radioactivity applied to PET studies with the irreversible monoamine oxidase A tracers [¹¹C]clorgyline and deuterium-substituted [¹¹C]clorgyline. *J Cereb Blood Flow Metab.* 2002;22:1367-1376.
21. Ploessl K, Wang L, Lieberman BP, Qu W and Kung HF. Comparative evaluation of ¹⁸F-labeled glutamic acid and glutamine as tumor metabolic imaging agents. *J Nucl Med.* 2012;53:1616-1624.
22. Hassanein M, Hight MR, Buck JR, et al. Preclinical Evaluation of 4-[¹⁸F]Fluoroglutamine PET to Assess ASCT2 Expression in Lung Cancer. *Mol Imaging Biol.* 2016;18:18-23.
23. Xu X, Zhu H, Liu F, et al. Imaging Brain Metastasis Patients With ¹⁸F-(2S,4R)-4-Fluoroglutamine. *Clin Nucl Med.* 2018;43:e392-e399.
24. Jin L, Chun J, Pan C, et al. The PLAG1-GDH1 Axis Promotes Anoikis Resistance and Tumor Metastasis through CamKK2-AMPK Signaling in LKB1-Deficient Lung Cancer. *Mol Cell.* 2018;69:87-99.
25. Rodrigues MF, Obre E, de Melo FH, et al. Enhanced OXPHOS, glutaminolysis and β -oxidation constitute the metastatic phenotype of melanoma cells. *Biochem J.* 2016;473:703-715.
26. Bröer A, Fairweather S and Bröer S. Disruption of Amino Acid Homeostasis by Novel ASCT2 Inhibitors Involves Multiple Targets. *Front Pharmacol.* 2018;9:785.
27. Hoerner CR, Chen VJ and Fan AC. The 'Achilles Heel' of Metabolism in Renal Cell Carcinoma: Glutaminase Inhibition as a Rational Treatment Strategy. *Kidney Cancer.* 2019;3:15-29.
28. Csibi A, Fendt SM, Li C, et al. The mTORC1 pathway stimulates glutamine metabolism and cell proliferation by repressing SIRT4. *Cell.* 2013;153:840-854.
29. Vajaitu C, Draghici CC, Solomon I, et al. The Central Role of Inflammation Associated with Checkpoint Inhibitor Treatments. *J Immunol Res.* 2018;2018:4625472.
30. Albina JE, Henry W, King PA, et al. Glutamine metabolism in rat skeletal muscle wounded with lambda-carrageenan. *Am J Physiol.* 1987;252:E49-56.

FIGURES

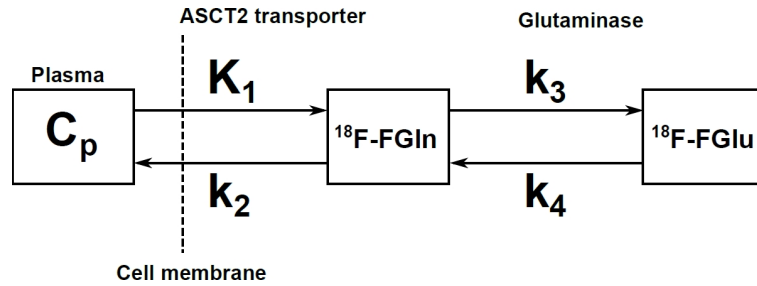


Figure 1. Schematic of the reversible 2-tissue compartment model with four kinetic rate constants (2C4K).

C_p is the plasma compartment, representing unmetabolized ^{18}F -FGln that is available for transport across the vasculature into tissue. The 1st compartment represents non-specifically bound ^{18}F -Fluoroglutamine that has been transported into tumor cells by ASCT2 and other transporters, whereas the 2nd compartment represents the activity from ^{18}F -fluoroglutamate, produced in the first and rate-limiting step of glutaminolysis that is catalyzed by glutaminase. For the descriptions of kinetic rate constants, please see text.

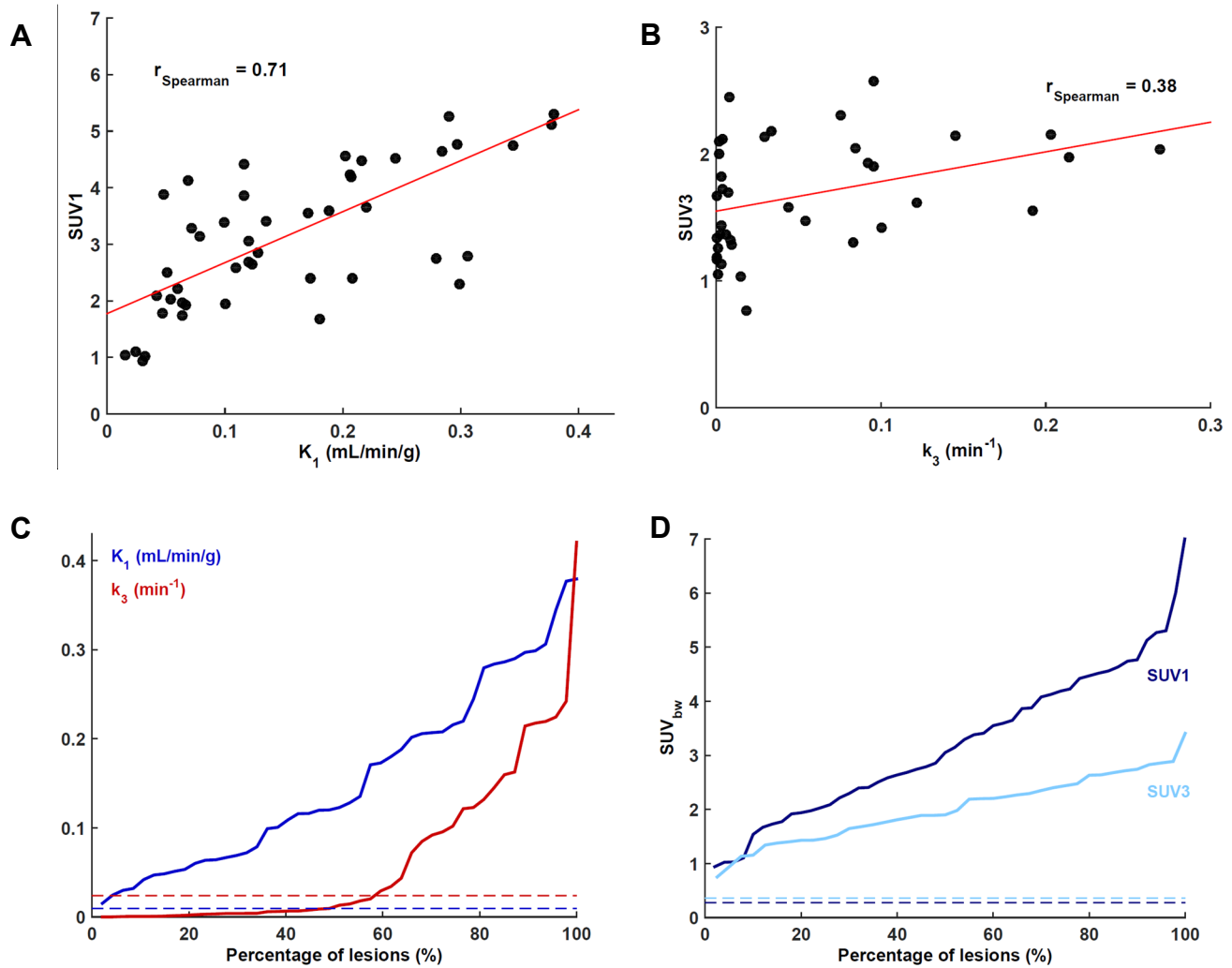


Figure 2. (A) Scatterplot of maximum intratumor K_1 -SUV1. K_1 was the kinetic rate constant most closely correlated with SUV1 (measured on the last dynamic 5-min frame, 25-30 min post-injection). (B) Scatterplot of maximum intratumor k_3 -SUV3. (C) Waterfall chart of maximum intratumor K_1 (blue) and k_3 (red). (D) Waterfall chart of maximum intratumor SUV1 (dark blue) and SUV3 (light blue). In both waterfall charts, average values for normal brain tissue are overlaid as color-coded dashed lines.

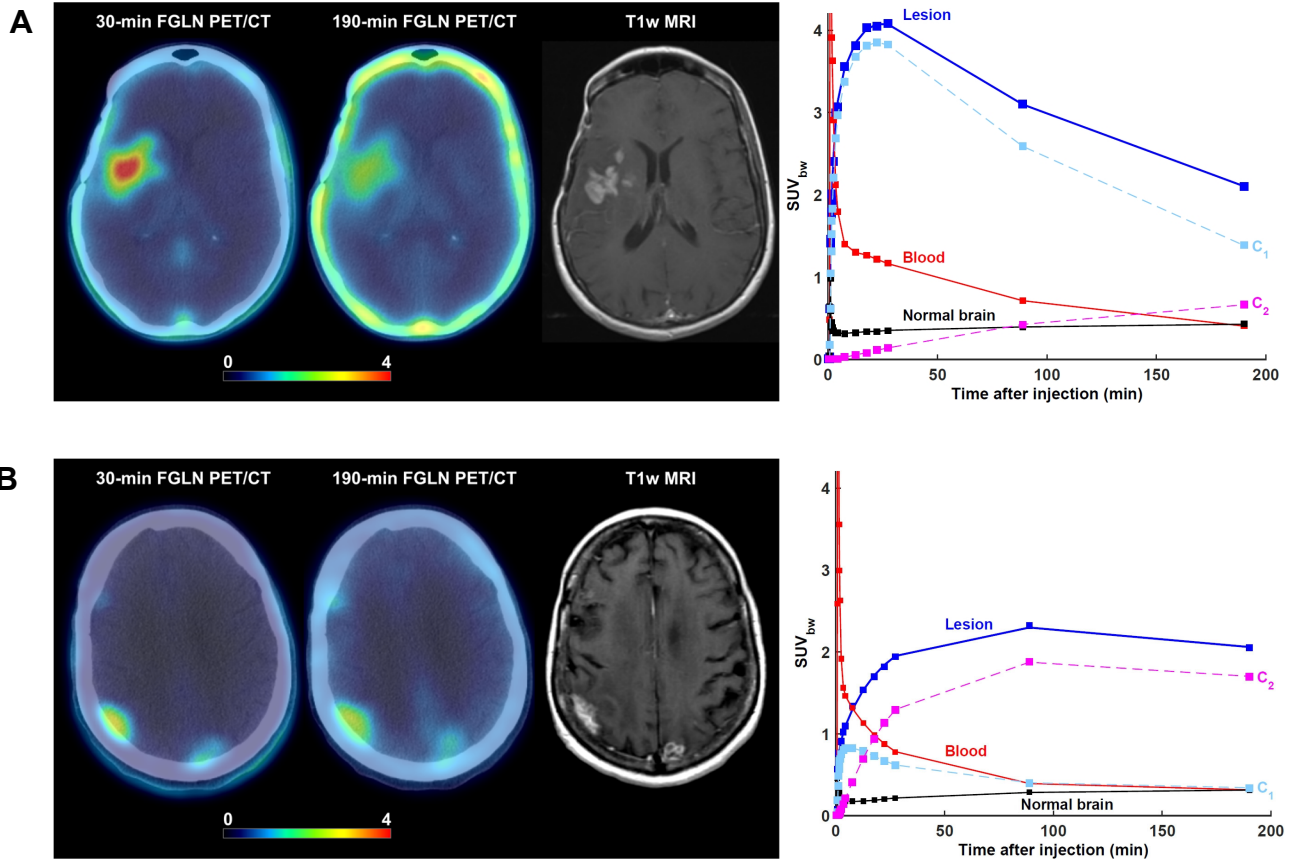


Figure 3. Lesions from two patients exhibiting different ^{18}F -FGln pharmacokinetics despite having very similar SUV_{bw} as measured at 190 min post-injection. In both cases, axial view of the last dynamic PET frame (5-min acquisition time, 25-30 min post-injection) and last imaging frame (\sim 190 min post-injection), fused with corresponding CT is displayed. Post-gadolinium contrast T1-weighted MRI is included for comparison. Three time-activity curves (TACs) shown are for whole tumor (blue); image-derived input function scaled by the whole-blood activity concentration as measured from blood samples, patient-specific plasma fraction, and population-based metabolite fraction (red); and normal brain tissue (black). Contributions to the total PET signal for tumor TACs are superimposed in light blue (first compartment; C_1) and purple (second compartment; C_2). (A) 52-year-old female patient with confirmed diagnosis of astrocytoma. ^{18}F -FGln PET/CT shows the 2 cm^3 lesion in the right frontotemporal region. Mean intratumor K_1 , k_2 , k_3 , k_4 , and V_T were 0.28 $\text{mL}/\text{min}/\text{g}$, 0.08 min^{-1} , 0.002 min^{-1} , 0.001 min^{-1} , and 3.9 mL/cm^3 , respectively. Corresponding values for normal brain tissue were 0.02 $\text{mL}/\text{min}/\text{g}$, 0.09 min^{-1} , 0.001 min^{-1} , 0.001 min^{-1} , and 0.5 mL/cm^3 , respectively. SUV_{bw} at 30 min, 90 min, and 190 min was 4.0, 3.1, and 2.1, respectively. At

these three time-points, the signal from the second compartment contributed 3%, 14%, and 32% of the total PET activity concentration. (B) 70-year-old female patient with confirmed diagnosis of non-small cell lung cancer that metastasized to brain. PET image shows the metastatic lesion in the right parietal region. Mean intratumor K_1 , k_2 , k_3 , k_4 , and V_T were 0.13 mL/min/g, 0.13 min⁻¹, 0.09 min⁻¹, 0.02 min⁻¹, and 5.1 mL/cm³, respectively. Corresponding values for normal brain tissue were 0.01 mL/min/g, 0.05 min⁻¹, 0.04 min⁻¹, 0.004 min⁻¹, and 0.7 mL/cm³, respectively. SU_w at 30 min, 90 min, and 190 min was 1.9, 3.1, and 2.1, respectively. At these three time-points, the signal from the second compartment contributed 66%, 82%, and 83% of the total PET activity concentration.

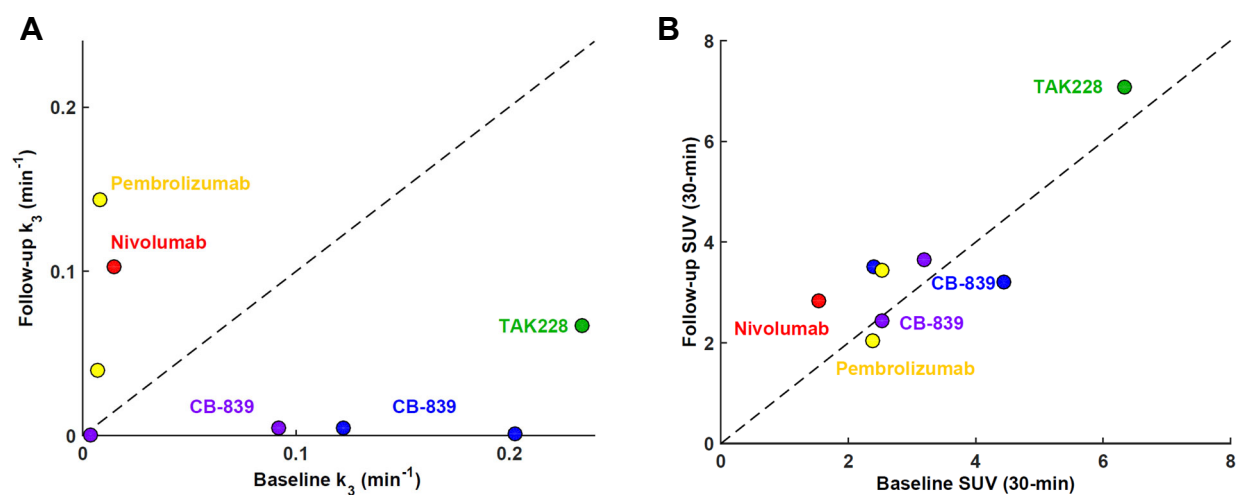


Figure 4. (A) Scatterplot of baseline versus follow-up mean intratumor k_3 for $n=5$ patients ($n=8$ lesions in total) who underwent two ¹⁸F-FGln dynamic PET scans. Every patient is color-coded and annotated according to the therapy received between baseline and follow-up ¹⁸F-FGln dynamic PET. Line of identity is superimposed as dashed line. (B) Corresponding scatterplot of baseline versus follow-up mean intratumor SUV as measured at 30-min post-injection.

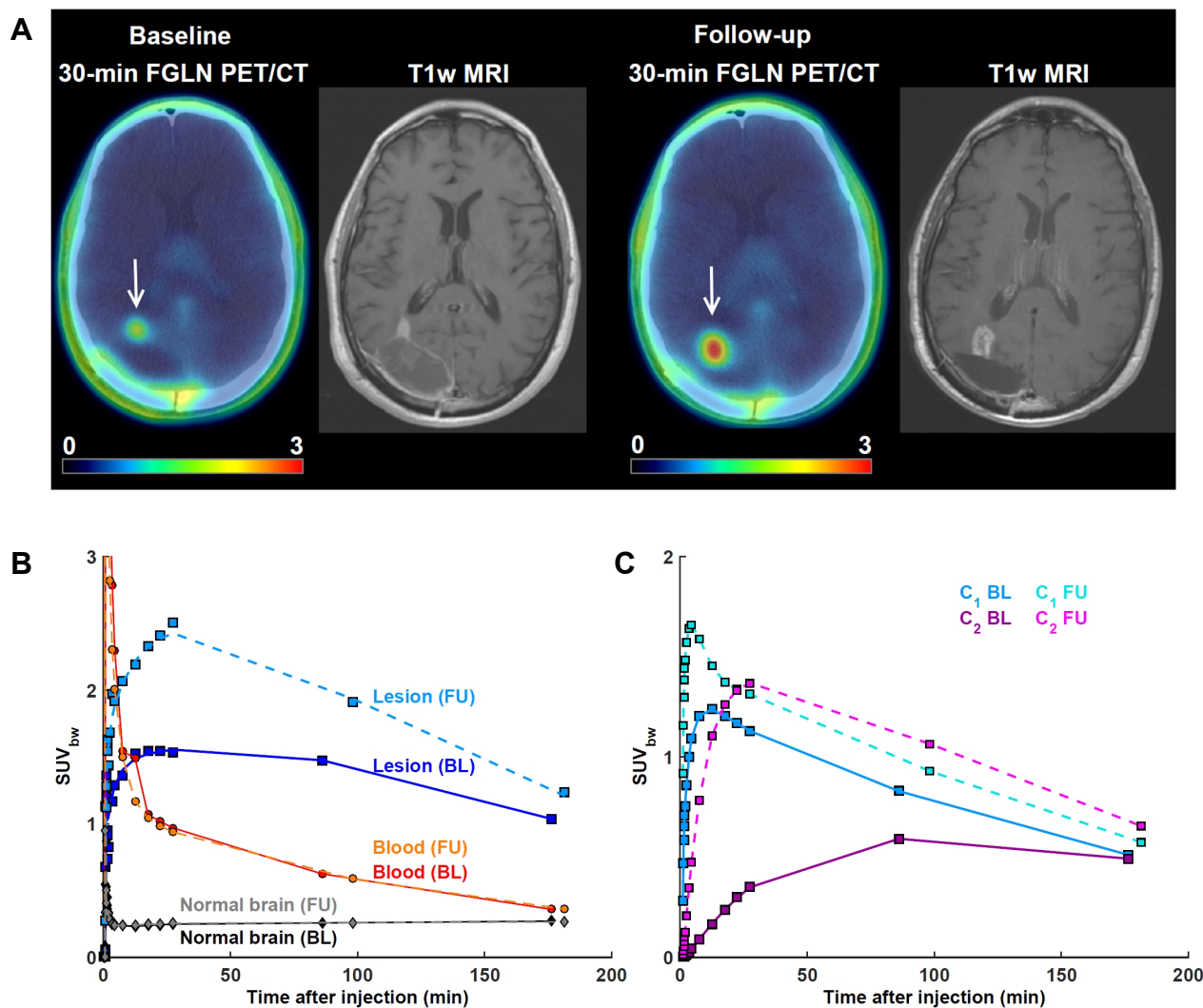


Figure 5. 68-year-old male patient with confirmed diagnosis of glioblastoma multiforme. (A) Left panel: baseline (first) ^{18}F -FGLN dynamic PET was performed post-right parietal occipital craniotomy for resection of the noted heterogeneously enhancing mass lesion centered in the right occipital lobe (white arrow). Right panel: follow-up (second) ^{18}F -FGLN dynamic PET performed 13 weeks after initiation of treatment with nivolumab and radiotherapy. Post-gadolinium contrast T1-weighted MRI scans were performed three and four days before the first and second ^{18}F -FGLN PET, respectively. When compared to the first MRI scan, the enhancing nodule extending toward the trigone of the right lateral ventricle on the second MRI scan is enlarged and exhibits higher ^{18}F -FGLN uptake at all imaging time-points. (B) Time-activity curves from first (baseline; BL) and second (follow-up; FU) ^{18}F -FGLN PET for tumor, image-derived input function scaled by the whole-blood activity concentration as measured from blood samples, patient-specific plasma fraction

and population-based metabolite fraction, and normal brain tissue. Mean intratumor K_1 , k_2 , k_3 , k_4 and V_T as calculated from first ^{18}F -FGln PET were 0.07 mL/min/g, 0.05 min⁻¹, 0.02 min⁻¹, 0.02 min⁻¹, and 2.1 mL/cm³, respectively. Corresponding values as calculated from 2nd ^{18}F -FGln PET were 0.16 mL/min/g, 0.11 min⁻¹, 0.10 min⁻¹, 0.10 min⁻¹, and 2.9 mL/cm³, respectively. (C) The signal from the second compartment contributed 23%, 40% and 47% of the total PET activity concentration at 30-min, 86-min and 176-min on the first scan and 50%, 53% and 53% at 30-min, 98-min and 182-min on the second scan.

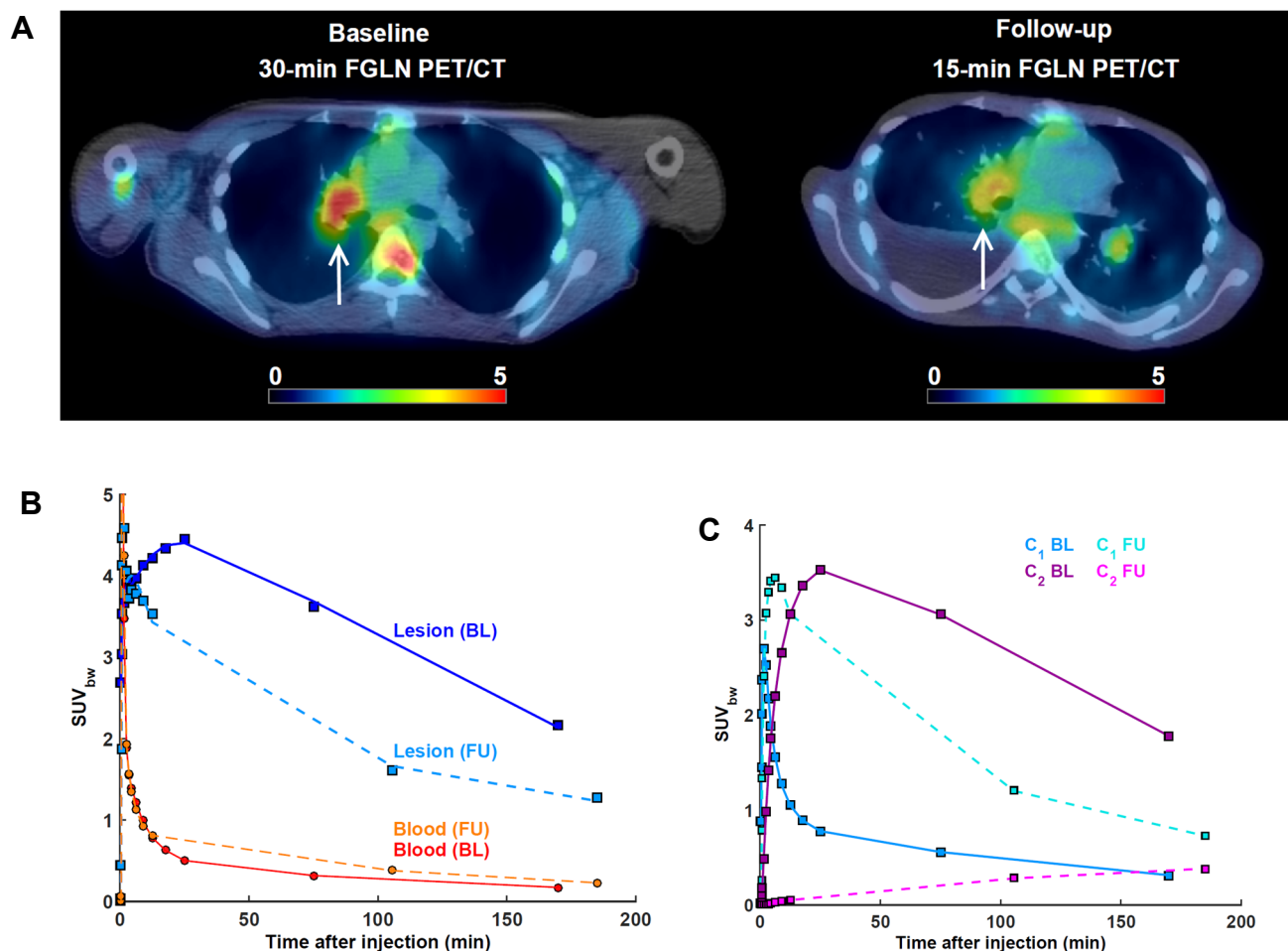


Figure 6. 23-year-old male patient with confirmed diagnosis of metastatic renal cell carcinoma. (A) Baseline (left panel) and follow-up (right panel) ^{18}F -FGLN dynamic PET, showing pulmonary metastasis in the right lung (white arrow). Follow-up scan was performed 4 weeks after initiation of therapy with glutaminase inhibitor CB-839. The acquisition was shortened to 15-min due to patient discomfort. (B) Time-activity curves from baseline (BL) and follow-up (FU) ^{18}F -FGLN PET for highlighted lesion and image-derived input function scaled by the whole-blood activity concentration as measured from blood samples, patient-specific plasma fraction and population-based metabolite fraction. Mean intratumor K_1 , k_2 , k_3 , k_4 and V_T as calculated from first ^{18}F -FGLN PET were 0.43 mL/min/g, 0.25 min $^{-1}$, 0.20 min $^{-1}$, 0.04 min $^{-1}$, and 9.1 mL/cm 3 , respectively. Corresponding values as calculated from 2nd ^{18}F -FGLN PET were 0.44 mL/min/g, 0.12 min $^{-1}$, 0.001 min $^{-1}$, 0.000 min $^{-1}$, and 4.4 mL/cm 3 , respectively. (C) The signal from the second compartment contributed 80%, 83% and 83% of the total PET activity concentration at 30-min, 75-min and 170-min on the first scan and 2%, 17% and 31% at 15-min, 105-min and 185-min on the second scan.

TABLES

Table 1. Subject demographics and clinical characteristics.

		N=41
Gender		
	Male	21
	Female	20
Age at baseline ¹⁸ F-FGln PET, y		
	<40	8
	40-49	6
	50-59	12
	60-69	8
	70-79	7
Cancer		
	Glioblastoma multiforme	14
	Astrocytoma	6
	Lung cancer	6
	Pancreatic cancer	4
	Breast cancer	3
	Oligodendroglioma	2
	Prostate cancer	2
	Colon cancer	1
	Ependymoma	1
	Diffuse large B cell lymphoma	1
	Renal cell carcinoma	1

Table 2. Summary of mean intratumor values for metrics derived from baseline ^{18}F -(2S,4R)-4-fluoroglutamine dynamic PET, as calculated with the reversible 2-compartment model (2C4K). Mean \pm standard deviation (range).

Metric	All lesions (n=50)	All brain lesions (n=35)	Primary brain lesions (n=26)	Brain metastases (n=9)	All thoracic / abdominal lesions (n=15)	Normal brain tissue (n=26)
SUV1	2.5 \pm 1.2 (0.6-6.3)	2.1 \pm 0.9 (0.6-4.0)	2.3 \pm 0.9 (0.6-4.0)	1.7 \pm 0.6 (0.6-2.9)	3.4 \pm 1.5 (1.4-6.3)	0.3 \pm 0.1 (0.2-0.4)
SUV2	2.2 \pm 0.9 (0.7-4.8)	2.1 \pm 0.7 (0.7-3.6)	2.1 \pm 0.7 (0.7-3.6)	2.0 \pm 0.6 (1.0-3.0)	2.5 \pm 1.2 (1.0-4.8)	0.3 \pm 0.1 (0.2-0.4)
SUV3*	1.7 \pm 0.5 (0.7-2.6)	1.6 \pm 0.5 (0.8-2.6)	1.6 \pm 0.5 (0.8-2.6)	1.9 \pm 0.4 (1.5-2.5)	1.8 \pm 0.5 (0.9-2.3)	0.4 \pm 0.1 (0.3-0.5)
V_B	0.07 \pm 0.05 (0.01-0.22)	0.06 \pm 0.04 (0.01-0.19)	0.05 \pm 0.04 (0.01-0.19)	0.07 \pm 0.04 (0.02-0.16)	0.10 \pm 0.07 (0.01-0.22)	0.03 \pm 0.01 (0.01-0.07)
K_1 (mL/min/g)	0.15 \pm 0.10 (0.02-0.42)	0.10 \pm 0.06 (0.02-0.24)	0.10 \pm 0.07 (0.02-0.28)	0.09 \pm 0.05 (0.02-0.15)	0.27 \pm 0.09 (0.18-0.42)	0.01 \pm 0.00 (0.00-0.01)
k_2 (min $^{-1}$)	0.11 \pm 0.11 (0.01-0.56)	0.06 \pm 0.06 (0.01-0.24)	0.06 \pm 0.05 (0.01-0.22)	0.08 \pm 0.07 (0.01-0.24)	0.21 \pm 0.14 (0.06-0.56)	0.05 \pm 0.04 (0.02-0.20)
k_3 (min $^{-1}$)	0.06 \pm 0.07 (0.00-0.27)	0.04 \pm 0.06 (0.00-0.21)	0.02 \pm 0.04 (0.00-0.15)	0.08 \pm 0.08 (0.01-0.21)	0.10 \pm 0.10 (0.00-0.27)	0.02 \pm 0.01 (0.01-0.04)
k_4 (min $^{-1}$)	0.02 \pm 0.03 (0.00-0.10)	0.02 \pm 0.02 (0.00-0.10)	0.01 \pm 0.02 (0.00-0.06)	0.03 \pm 0.03 (0.00-0.10)	0.03 \pm 0.03 (0.00-0.10)	0.003 \pm 0.003 (0.000-0.009)
V_T (mL/cm 3)	3.7 \pm 1.7 (1.8-10.0)	3.6 \pm 1.6 (1.8-10.0)	3.3 \pm 1.6 (1.8-10.0)	4.3 \pm 1.4 (2.8-7.0)	4.2 \pm 2.0 (2.0-9.1)	0.6 \pm 0.2 (0.3-1.3)

SUV1, SUV2, SUV3 - standardized uptake value, corrected by body weight, as calculated from the last 5-min frame of the 30-min dynamic acquisition, ~100-min and ~190-min PET acquisitions, respectively. V_T - Volume of distribution (Logan graphical analysis).

*SUV3 was not measured in n=10 lesions.

Table 3. Spearman's ρ between metrics derived from dynamic data (2C4K model) and SUV_{max} for the small intratumor area of highest ^{18}F -(2S,4R)-4-fluoroglutamine uptake

	30 min (SUV1)	100 min (SUV2)	190 min (SUV3)	$\Delta(SUV3-SUV1)$
K_1	0.71	0.63	0.51	-0.65
k_2	0.38	0.36	0.48	-0.28
k_3	0.13	0.25	0.38	0.13
k_4	0.14	0.26	0.26	-0.10
V_T	0.48	0.61	0.53	-0.27

2C4K - Reversible 2-tissue compartment model. SUV_{max} - maximum tumor standardized uptake value corrected by body weight. V_T - Volume of distribution (Logan graphical analysis).

Table 4. Reproducibility of metrics derived from truncated 30 min ^{18}F -(2S,4R)-4-fluoroglutamine dynamic PET compared to full 3h dataset. Kinetic rate constants were derived using the 2C4K model.

Metric	ICC	Mean difference (LoA)
K_1 (mL/min/g)	0.96	-0.01 (-0.07, 0.05)
k_2 (min^{-1})	0.63	-0.03 (-0.20, 0.15)
k_3 (min^{-1})	-0.01	-0.06 (-0.42, 0.30)
k_4 (min^{-1})	-0.09	-0.03 (-0.21, 0.15)
Volume of distribution (mL/cm ³)	0.75	0.90 (-0.77, 2.57)

2C4K - Reversible 2-tissue compartment model. ICC - Intraclass Correlation Coefficient, LoA - Limits of Agreement (lower, upper).

Table 5. Treatment information for patients that underwent second ^{18}F -(2S,4R)-4-fluoroglutamine dynamic PET.

Patient #	Cancer	Therapy	Time between 1 st and 2 nd PET (days)	Dosing
1	Renal cell carcinoma	CB-839	55	400 mg 3x daily
2	Non-small cell lung cancer	CB-839	27	400 mg 3x daily
3	Glioblastoma multiforme	Nivolumab + Radiotherapy	92	200 mg 1x daily
4	Glioblastoma multiforme	Pembrolizumab	68	200 mg 1x daily
5	Glioblastoma multiforme	TAK-228	49	3 mg 1x daily*

FOV - Field of view for the dynamic PET scan. *patient self-discontinued the trial after 1 month.

Table 6. Summary of mean intratumor values for metrics derived from early response ^{18}F -(2S,4R)-4-fluoroglutamine dynamic PET scans with the 2C4K model. Mean \pm standard deviation (range).

Metric	All lesions (n=8)	Corresponding n=8 lesions on baseline
SUV1	3.5 \pm 1.5 (2.0-7.1)	3.2 \pm 1.5 (1.8-6.3)
SUV2	3.0 \pm 1.2 (2.0-5.7)	2.8 \pm 1.1 (1.5-4.8)
V_B	0.17 \pm 0.10 (0.03-0.30)	0.12 \pm 0.06 (0.04-0.19)
K_1 (mL/min/g)	0.21 \pm 0.16 (0.04-0.46)	0.23 \pm 0.12 (0.07-0.43)
k_2 (min^{-1})	0.09 \pm 0.04 (0.03-0.13)	0.15 \pm 0.10 (0.04-0.30)
k_3 (min^{-1})	0.05 \pm 0.06 (0.00-0.14)	0.09 \pm 0.09 (0.00-0.23)
k_4 (min^{-1})	0.03 \pm 0.03 (0.00-0.10)	0.02 \pm 0.02 (0.00-0.06)
V_T (mL/cm 3)	3.4 \pm 1.5 (1.3-5.6)	4.7 \pm 2.2 (2.2-9.1)

2C4K - Reversible 2-tissue compartment model. SUV1, SUV2 - standardized uptake value, corrected by body weight, as calculated from the last 5-min frame of the 30-min dynamic acquisition and ~100-min PET acquisitions, respectively. SUV3 is not reported as only 2 patients had a ~190-min post-injection acquisitions on both first and second ^{18}F -FGln dynamic PET. V_T - Volume of distribution (Logan graphical analysis).

Supplementary Data

Monte Carlo simulations

Monte Carlo simulations were performed within PMOD software for a subset of time-activity curves derived from four patients presented in Figures 3, 5 and 6 in the manuscript. In each case, patient-specific input function was used that has been corrected for plasma fraction (also patient-specific) and metabolite fraction (population-based correction). The target activity concentration at each time frame was weighed by

$$w_i = \frac{1}{\sigma_i^2}, \quad \sigma_i = c\sqrt{\left(\frac{AC(t_i)}{\Delta t_i \times e^{-\lambda t_i}}\right)}, \quad (1)$$

where c is the scaling factor, Δt_i is the frame duration, $AC(t_i)$ is the decay-corrected activity concentration measured at the mid-frame time t_i , and $\lambda = \ln 2 / T_{1/2}$ is the isotope decay constant. The scale factor used was calculated from phantom experiment data, as published previously (32), taking into account the tumor size. The “true” parameters were used as starting values. After 100 fits of noisy data were performed, the distribution of the result parameters was analyzed resulting in a mean and a standard deviation value for each fitted parameter.

The mean from the 100 samples was within 1% of the “true” parameter value for all kinetic rate constants in all cases. The variance in the calculated kinetic rate constants was 1-5% for K_1 , 2-15% for k_2 , 2-30% for k_3 and 4-50% for k_4 . Larger variance for k_3 and k_4 was observed for the lesion shown in Figure 3A, for which “true” k_3 and k_4 were very low, being 0.002 min^{-1} and 0.001 min^{-1} , respectively.

Supplementary References

32. Grkovski M, Schwartz J, Gonen M, et al. Feasibility of ^{18}F -Fluoromisonidazole Kinetic Modeling in Head and Neck Cancer Using Shortened Acquisition Times. *J Nucl Med*. 2016;57:334-41.

Supplementary Table S1. Summary of values for metrics derived from a small region of interest (5 voxels) focused on the area of maximum ^{18}F -(2S,4R)-4-Fluoroglutamine uptake on baseline PET. Mean \pm standard deviation (range).

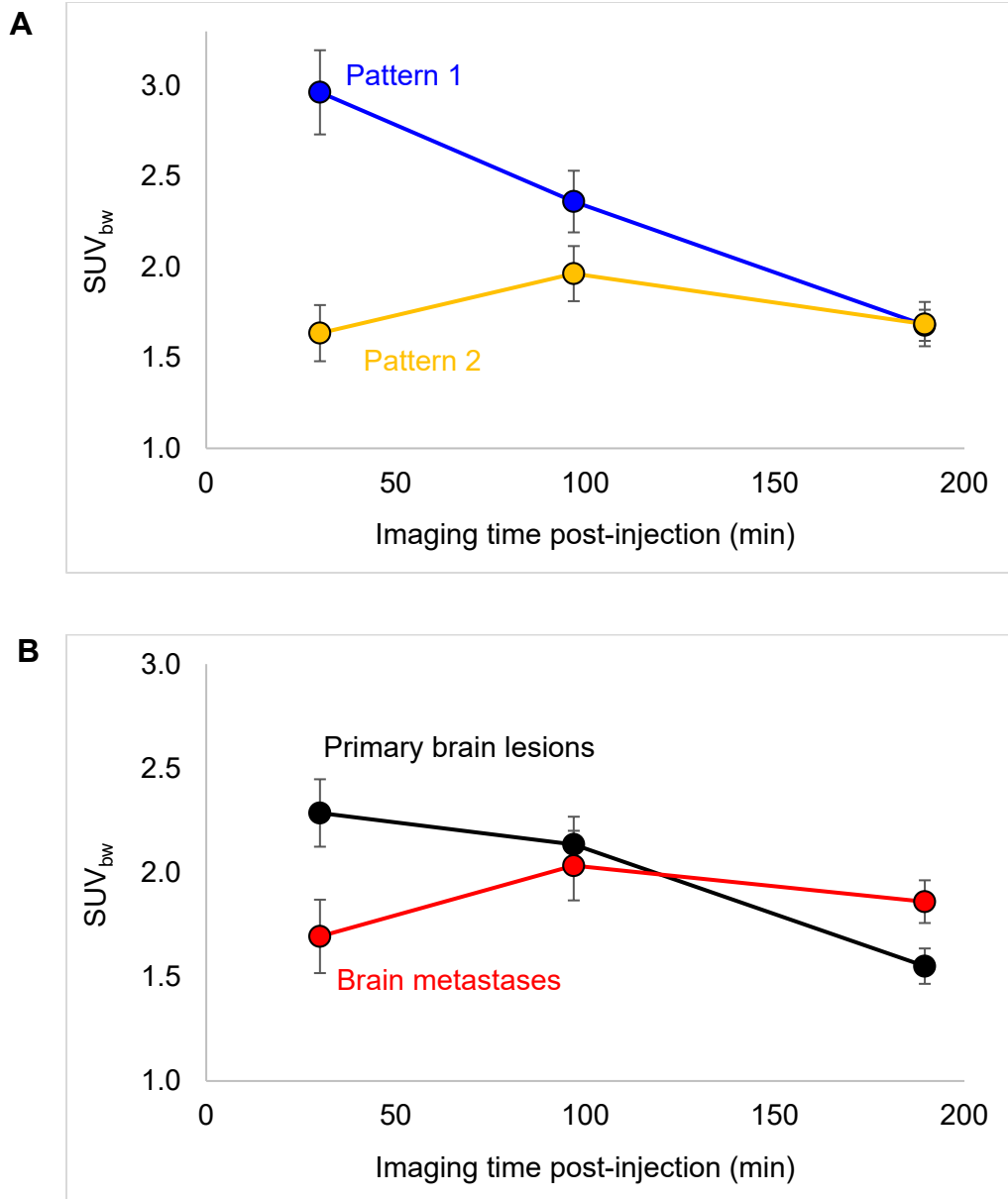
Metric	All lesions (n=50)	All brain lesions (n=35)	Primary brain lesions (n=26)	Brain metastases (n=9)	All thoracic / abdominal lesions (n=15)
SUV1	3.2 \pm 1.4 (0.9-7.1)	2.9 \pm 1.2 (0.9-5.1)	3.1 \pm 1.2 (0.9-5.1)	2.4 \pm 1.0 (1.0-4.2)	3.9 \pm 1.7 (1.5-7.1)
SUV2	2.8 \pm 1.1 (0.8-5.6)	2.7 \pm 0.9 (0.8-4.6)	2.6 \pm 0.9 (0.8-4.6)	2.8 \pm 0.7 (2.0-3.6)	3.1 \pm 1.6 (0.8-5.6)
SUV3*	2.0 \pm 0.6 (0.8-3.4)	2.0 \pm 0.6 (0.9-3.4)	2.0 \pm 0.7 (0.9-3.4)	2.2 \pm 0.5 (1.6-2.9)	2.1 \pm 0.8 (0.8-3.4)
v_B	0.07 \pm 0.05 (0.01-0.25)	0.06 \pm 0.05 (0.01-0.25)	0.06 \pm 0.05 (0.01-0.25)	0.07 \pm 0.04 (0.02-0.16)	0.10 \pm 0.06 (0.01-0.19)
K_1 (mL/min/g)	0.16 \pm 0.10 (0.02-0.38)	0.12 \pm 0.09 (0.015-0.38)	0.12 \pm 0.10 (0.02-0.38)	0.11 \pm 0.06 (0.03-0.21)	0.26 \pm 0.06 (0.18-0.38)
k_2 (min $^{-1}$)	0.10 \pm 0.10 (0.01-0.46)	0.07 \pm 0.06 (0.01-0.24)	0.06 \pm 0.06 (0.01-0.23)	0.10 \pm 0.06 (0.04-0.24)	0.19 \pm 0.11 (0.06-0.46)
k_3 (min $^{-1}$)	0.07 \pm 0.09 (0.00-0.42)	0.05 \pm 0.07 (0.00-0.24)	0.03 \pm 0.06 (0.00-0.22)	0.11 \pm 0.08 (0.01-0.24)	0.11 \pm 0.12 (0.00-0.42)
k_4 (min $^{-1}$)	0.04 \pm 0.08 (0.00-0.51)	0.04 \pm 0.09 (0.00-0.51)	0.04 \pm 0.10 (0.00-0.51)	0.03 \pm 0.02 (0.01-0.09)	0.04 \pm 0.04 (0.00-0.13)
V_T (mL/cm 3)	4.1 \pm 1.9 (1.8-11.2)	3.9 \pm 1.8 (1.8-11.2)	3.8 \pm 1.8 (1.8-11.2)	4.5 \pm 1.4 (3.0-7.6)	4.4 \pm 2.4 (1.8-10.7)

SUV1, SUV2, SUV3 - standardized uptake value, corrected by body weight, as calculated from the last 5-min frame of the 30-min dynamic acquisition, ~100-min and ~190-min PET acquisitions, respectively. V_T - Volume of distribution (Logan graphical analysis).
 *SUV3 was not measured in n=10 lesions.

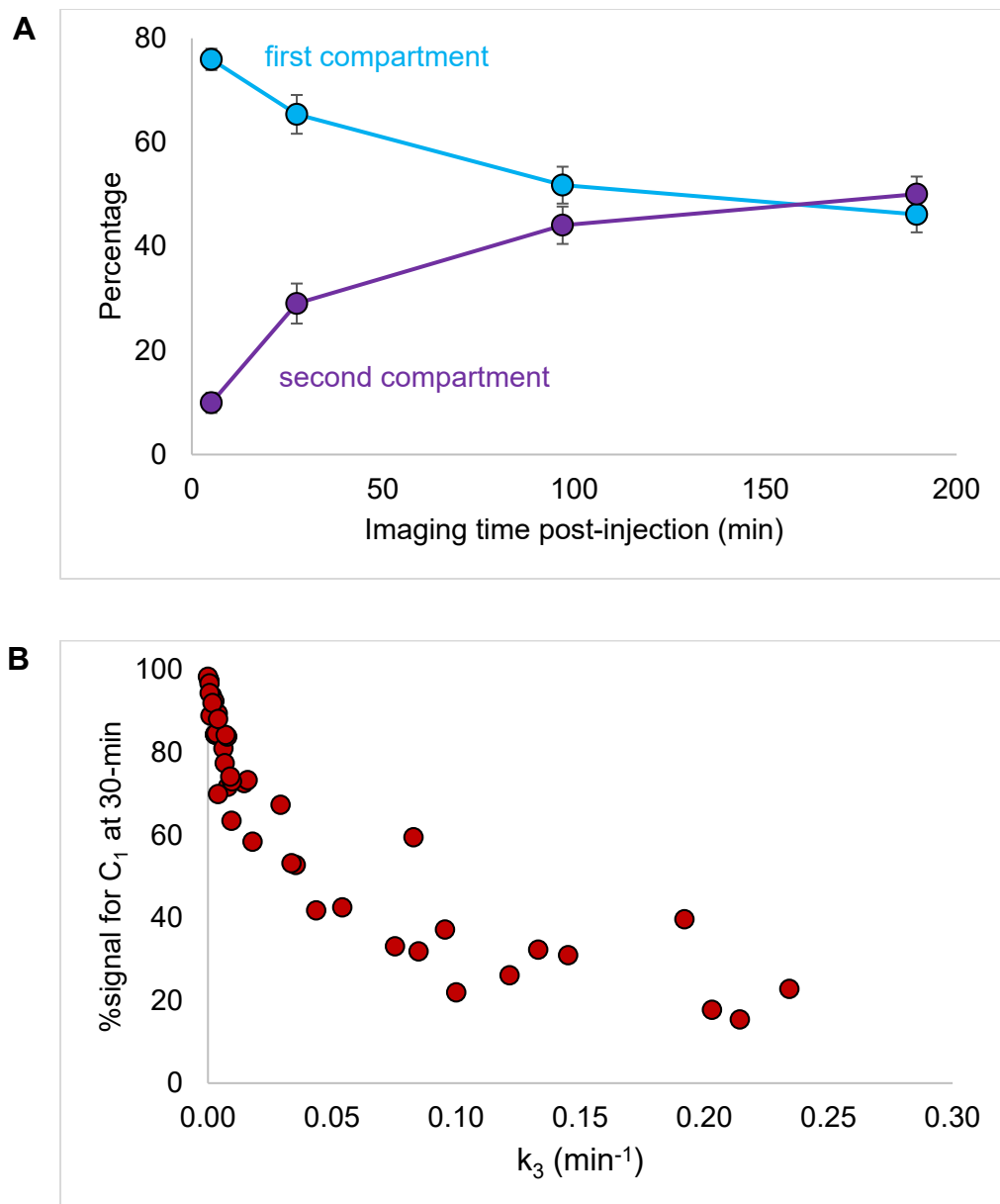
Supplementary Table S2. Spearman's ρ between kinetic rate constants from 2C4K model and V_T for all n=50 lesions.

	k_2	k_3	k_4	V_T
K_1	0.82	0.43	0.42	0.48
k_2		0.77	0.70	0.23
k_3			0.88	0.21
k_4				0.24

V_T - Volume of distribution (Logan graphical analysis).



Supplementary Figure S1. (A) Continuing decrease in ^{18}F -FGln uptake after 30-min imaging time-point was observed in 29/42 evaluable lesions (69%; Pattern 1. SUV1 = 3.0 ± 1.3 , SUV2 = 2.4 ± 0.9 and SUV3 = 1.7 ± 0.5), whereas a peak at ~100-min imaging time-point and a subsequent decrease was observed in the remaining 13/42 lesions (31%; Pattern 2. SUV1 = 1.6 ± 0.5 , SUV2 = 2.0 ± 0.5 and SUV3 = 1.7 ± 0.4). (B) Primary brain lesions (n=26) exhibited higher ^{18}F -FGln uptake after 30-min which subsequently decreased. ^{18}F -FGln uptake pattern in brain metastases (n=9) was markedly different, exhibiting a slower initial accumulation and a more sustained peak due to higher rate of glutaminolysis. Mean \pm Standard Error.



Supplementary Figure S2. (A) Percentage contributions to total PET signal from first (C₁) and second (C₂) compartment as a function of imaging time post-injection averaged over all n=50 lesions. Mean \pm Standard Error. (B) Scatterplot of mean intratumor k_3 as percentage signal from 1st compartment, as measured at 30-min post-injection. Spearman's $\rho = -0.97$.